International Journal of Rock Mechanics & Mining Sciences 154 (2022) 105124

Contents lists available at ScienceDirect

International Journal of Rock Mechanics and Mining Sciences

journal homepage: www.elsevier.com/locate/ijrmms

Stress modelling using cellular automata for block caving applications

René Gómez [a,*], Raúl Castro [b]

[a] Universidad de Concepción, Chile
[b] Universidad de Chile, Chile

ARTICLE INFO

Keywords:
Caving
Cellular automata
Granular material
Gravity flow
Stress modelling

ABSTRACT

In underground mining, rock mass stress is commonly modeled as a continuum. However, in block cave mining discrete modelling should be used to properly represent the stress over the extraction level in the broken column where there are high rock columns of large rock fragments. Unfortunately, we lack methods that use discrete modelling of stress in the broken column at block caving scale. In this work, we propose a vertical stress model of granular material to simulate static and dynamic flow conditions. The model is developed within a gravity flow simulator based on cellular automata to simulate the scale of the problem and flow conditions. The vertical stress model proposed is calibrated through four experimental models for the static condition. Then, based on the results from experimental testing, the dynamic condition is calibrated and compared with different flow scenarios. The results show that the proposed model can correctly simulate the vertical stresses in static conditions as well as dynamic conditions under the different flow setups tested. This vertical stress model with its flow simulator based on cellular automata has the potential to be applied at block caving scale once calibration parameters are defined.

1. Introduction and literature review

Studies of stress in granular material have been carried out for many years due to this material's importance in many industries (i.e. Food, Pharmacy, Mining[1–3]). In block cave mining, the granular material is composed of large rock fragments within a broken column of hundreds of meters. Thus, a soil mechanics approach has been proposed to estimate stress in the caved column,[4–7] using the corrected classic Janssen approach[8] as an initial stress estimation. Nevertheless, the stress modelling of a broken column is more complex when different rock types, draw strategies, and complex cave geometries have to be considered.

A common tool used to study complex granular media problems is the distinct element method (DEM;[9]), frequently used in stress studies (e.g:[10–17]). DEM has also been used in mining studies.[18–21] However, in cave mining studies,[19–21] the problems have been limited to a drawbell, a short column height and simplified shape fragments because of the problem of scale. As an example in Ref. 21, a draw simulation of a cylindrical model of 0.7 m height and 0.34 m diameter takes between a week and a month to complete. Other numerical tools are used for large scale problems that quickly simulate the ore flow without considering dynamic interaction between particles, such as PCBC,[22] CAVESIM,[23] FLOWSIM,[24] and REBOP.[5]

Stress has also been measured in the extraction level of block cave mines[25–27] with different techniques for field stress measurement such as stress cells, over-coring, the Flat Jack test, and hydraulic fracturing.[28,29] Rojas et al.[25] used stress cells in the Esmeralda mine (within the El Teniente mine) and identified the need for production pillar rehabilitation after abutment stress to provide support during ore extraction. Xia et al.[27] also studied the stability of the extraction level before and after undercutting in the Tongkaungyu mine using over-coring. In this mine, the stability problems mainly occurred during the undercutting, but stability problems were also reported during ore extraction. Additionally, indirect techniques have been applied. Martin et al.[30] proposed stress model calibration based on the drift damage and the depth of failure, while Gonzales et al.[31] used the damage observed in borehole cameras to model stress. In the Deep Ore Zone mine, they measured production drift convergence,[32] where stress concentration during ore extraction was observed. Another indirect technique was proposed by Xia et al.[33] to estimate stress in the extraction level through the thin plate theory.

During ore extraction induced stress is, directly or indirectly, observed in the extraction level. Moreover, damage from stress has been reported in this level.[6,34,35] Stress measurement is useful during mining; however, it would also be useful to estimate stress in previous stages.

* Corresponding author.
E-mail address: regomez@udec.cl (R. Gómez).

https://doi.org/10.1016/j.ijrmms.2022.105124
Received 15 November 2021; Received in revised form 9 March 2022; Accepted 8 April 2022
Available online 25 April 2022

List of symbols

2D	Two dimensions	H	Model height
3D	Three dimensions	h_i	Height of movement zone
βi	Weight distribution function	IMZ	Isolated movement zone
φ_w :	Friction wall [°]	MZ	Movement zone
σ_v	vertical stress	n	number of cells in vertical axis
σ_{v0}	Initial vertical stress	P_i	Weight
γ_i	specific gravity	P_T	Total weight
CA	Cellular automata	P_V	vertical weight transmitted
DEM	Distinct element method	R	Relaxation parameter
d_{ij}	distance between cell i and j	s	Stress model parameter (in stagnant and/or movement zone)
B	Stress model parameter in stagnant zone	V	Cell volume
B_{min}	Stress model parameter in movement zone	W_r	Stagnant zone width
		W_i	Movement zone width

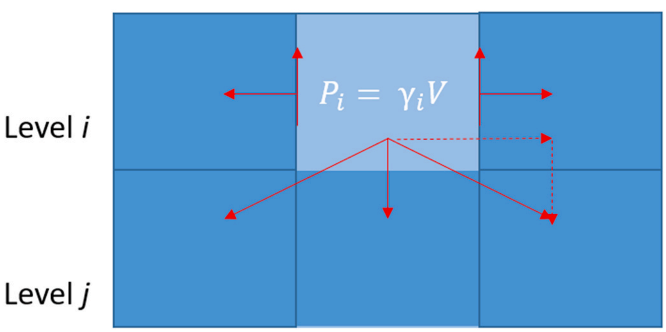

Fig. 1. Profile view (2D) of weight transmission in a cell lattice, the red arrows represent the force transmissions of a cell. (For interpretation of the references to color in this figure legend, the reader is referred to the Web version of this article.)

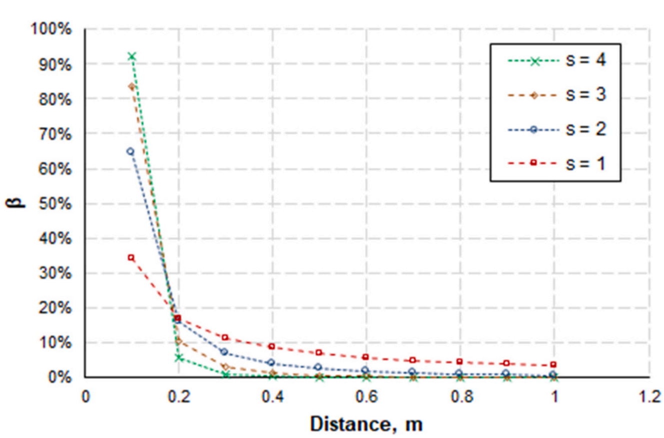

Fig. 2. Effect of s on the force distribution parameter.

DEM are not preferable yet for full block cave scales because of the time required for simulation. Thus, in this work we propose to incorporate a vertical stress model in a gravity flow simulator based on cellular automata (CA) that will be able to quickly model vertical stress in high draw columns under different draw scenarios.

2. Stochastic stress model through cellular automata

Granular media can be described by stochastic interactions[36] mainly due to their random shapes, sizes, contact points and contact forces.[37] However, this randomness follows a degree of regularity, which has allowed stochastic models of granular material flow[36,38–41] and stress in granular material[42–44] to be developed.

In mining, the stochastic rules used for gravity flow have been applied through Cellular Automata (CA).[23,24,45–52] Gravity flow modelling with CA is based on the void diffusion mechanism.[53] This mechanism has been identified in Block and Sublevel caving mines,[54–59] including in fine material fragmentation (<0.4 mm[60]). CA have also been used for a wide variety of complex matter in models such as rough annular shear cells, lattice-gas, lattice-grain, hybrid models, movable CA, elasto-plastic rock failure, Continuous-discontinuous CA and.[61–69]

In granular materials, the stresses are transmitted by chain forces due to the media inhomogeneity,[42,70] that generates stochastic stress distribution. Liu et al.[42] and Coppersmith et al.[43] proposed stress modelling in granular material by CA, through stochastic weight transmitted downward between particles, without considering the coordination number. Then, Hemmingsson et al.[44] applied force vectors to model the vertical forces transition reporting favorable results in silo and heap geometries of granular material.

In this work, we applied the weight transition through cells in a CA to simulate gravity flow in caving mines.[47,52] The gravity flow propagated during ore extraction was simulated using the void diffusion concept. The voids are inserted in draw points and have a probability of moving upwards and exchanging location with a non-void (granular) cell. Inversely, the weight of a (granular) cell is distributed randomly among lower cells (as shown in Fig. 1 in 2D). The weight is distributed only over non-void cells. In Fig. 1, a cell in the i level distributed its weight, P_i, over a lower cell in the j level. The weight is a function of the specific gravity, γ_i, and the cell volume, V. Additionally, shear forces (by friction) and horizontal forces could be considered. However, in this work only vertical force transmission was modeled. The vertical stress model was applied in a cubic lattice of cells where a cell distributed its weight over 9 lower cells (in 3D).

The vertical forces in the model are the weight components (by gravity) and the shear components (by friction). The shear components support part of the individual cell's weight. Here, we simplified the weight transmission introducing a buoyant parameter, E, that represents the weight fraction of a cell that is distributed to lower cells. Then, $1 - E$ is the cell's weight fraction that is supported by friction. The cell's weight distributed to lower cells is represented by Eq. (1).

$$\gamma_i - \gamma i \cdot (1 - E) = \gamma i \cdot E \quad E = \{0, 1\} \tag{1}$$

Then, the weight of a cell in level j is its weight plus the weight fractions of the nine upper cells (in 3D; Eq. (2)).

$$P_j = \gamma_j V + E \sum_{i=1}^{9} P_i \beta_i \tag{2}$$

P_j is the weight of cell j and βi is the weight fraction of the cell i

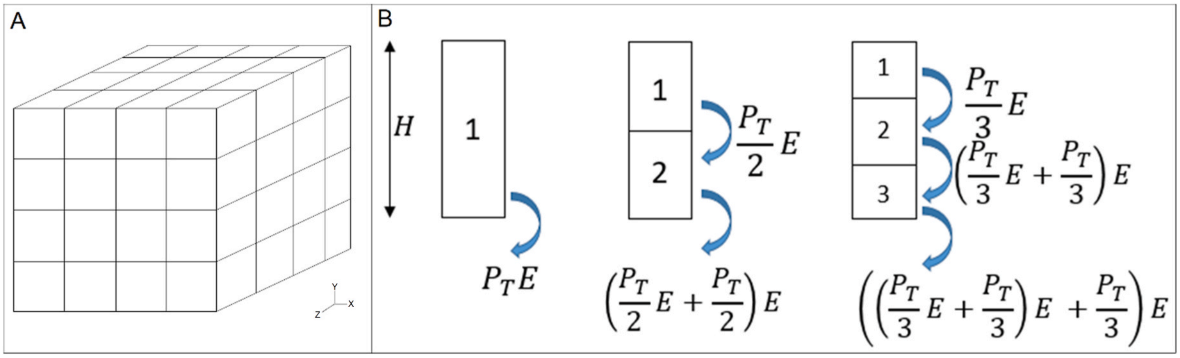

Fig. 3. A: Cubic cell lattice. B: Cumulative effect of parameter E as function of the cell lattice and model height.

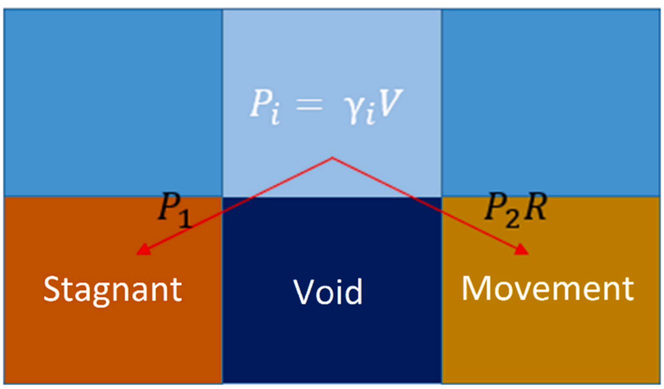

Fig. 4. Profile view (2D) of mass transmission in a six-cell arrangement with stagnant and movement zones (cells).

transmitted to cell j. βi is defined by the multinomial probability distribution in Eq. (3),

$$\beta(x_j) = \frac{n!}{\prod_{j=1}^{k} x_j!} \prod_{j=1}^{k} p_j^{x_j} \tag{3}$$

where $k = \{1, \ldots, 9\}$, $x_j = d_{ij}$ is the distance between cells i and j, n is the sum of the nine distances as $n = \sum_{j=1}^{k} x_j$, and p_j are the initial probabilities of the nine cells defined here as an inverse function of the distance (Eq. (4)), similar to the void diffusion rule used in the flow simulator.[47]

$$p_j = \frac{\left(1/d_{ji}\right)^s}{\sum \left(1/d_{ji}\right)^s} \tag{4}$$

In Eq. (4), s is a model parameter that must be calibrated. The influence of this parameter on the force distribution (β_i) is shown in Fig. 2 as a function of the distance between cells.

As can be observed in Fig. 2, the weight fraction received from upper cells decreased for larger distances between cells. The weight fraction distributed near the model boundary is omitted as was proposed by Hemmingsson et al.[44] because the wall friction (at the boundary) generates equal force in opposite directions. Additionally, the weight supported by nearby cells increases when s increases. Higher variability could be added to the model using a random s. However, this variability should not highly influence the mean vertical stress calculated in a level.

2.1. Cell lattice influence

The gravity flow simulator used a cubic cell lattice (Fig. 3A), in which the cell weight is transmitted level by level through the Y direction applying the buoyant parameter E. Then, the cell size and the total height both influence the vertical stress transmitted to the next lower level for a specific E value. This influence is shown in Fig. 3B for a fixed height (H). There is a cumulative effect of the E parameter when the cell weight is transmitted: the total weight, P_T, transmitted at the very bottom is decreased based on the number of cells in the vertical axis due to the parameter E.

Using the stress model, the weight calculated at the bottom, P_V, can be related to the total system weight, P_T, and to the number of cells in the vertical axis, n, as shown in Eq. (5).

$$Pv = \sum_{i=1}^{n} \frac{P_T}{n} E^{(i)} \xrightarrow{n\to\infty} P_T ln\left(\frac{1}{1-E}\right) = P_T \frac{E}{n} \frac{1-E^n}{1-E} \tag{5}$$

2.2. Stress modelling during gravity flow

The proposed stress model is defined for static granular material. However, as we have seen in previous studies, vertical stress increases in the stagnant zones and decreases in the movement zones when gravity flow begins due to ore extraction.[4,5,7,19] One reason is that the movement zones have less bulk density,[71–73] decreasing the contact points between particles for force transmission. In our stress model, we introduce a relaxation parameter, R (between 0 and 1), to model the weight distribution between the movement and stagnant zones. This parameter should depend on the rock properties and system geometry. The R parameter decreases the probability of weight distribution over the movement zone when there is a cell (or more) located in the stagnant zone (Fig. 4). The weight distribution of a cell, defined by Eq. (3), over a cell in the movement zone is multiplied by R to decrease the weight transmitted over this cell. The weight distribution defined by β_i must sum 100% to avoid weight losses for this rule, assuming that $P_1 + P_2R = 100\%$ (in Fig. 4 example for 2D). The weight is distributed mainly over the stagnant zones by including this R parameter.

Additionally, the height of the model influences E (as described in section 2.1). Thus, the movement zone height also influences E. Then, we defined E_{min}, for the buoyant parameter in the movement zone that depends on the movement zone height. Finally, the parameters R and E_{min} are used to model stress under flow conditions.

3. Experimental methodology

Four physical models were simulated in the gravity flow simulator applying the stress model. The vertical stress measurements obtained from the physical models were then used to calibrate the parameter E in the static condition. The physical model of Castro et al.[7] was selected to calibrate the parameters E_{min} and R because in this model different flow scenarios were tested. Finally, the numerical model calibrated in static and dynamic conditions was compared with different flow scenarios. Python V3.7 was used in this work to build the CA stress model.

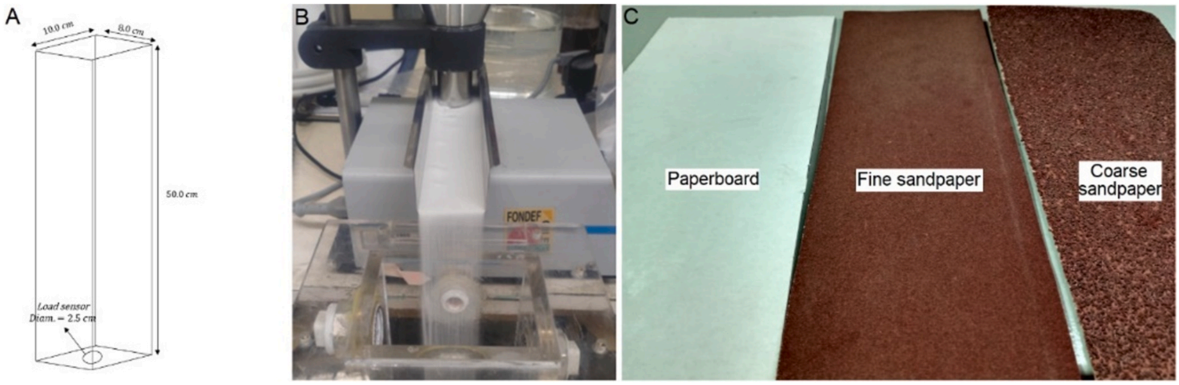

Fig. 5. A: Column model dimensions. B: Feeder system used to fill the model. C: Wall's material.

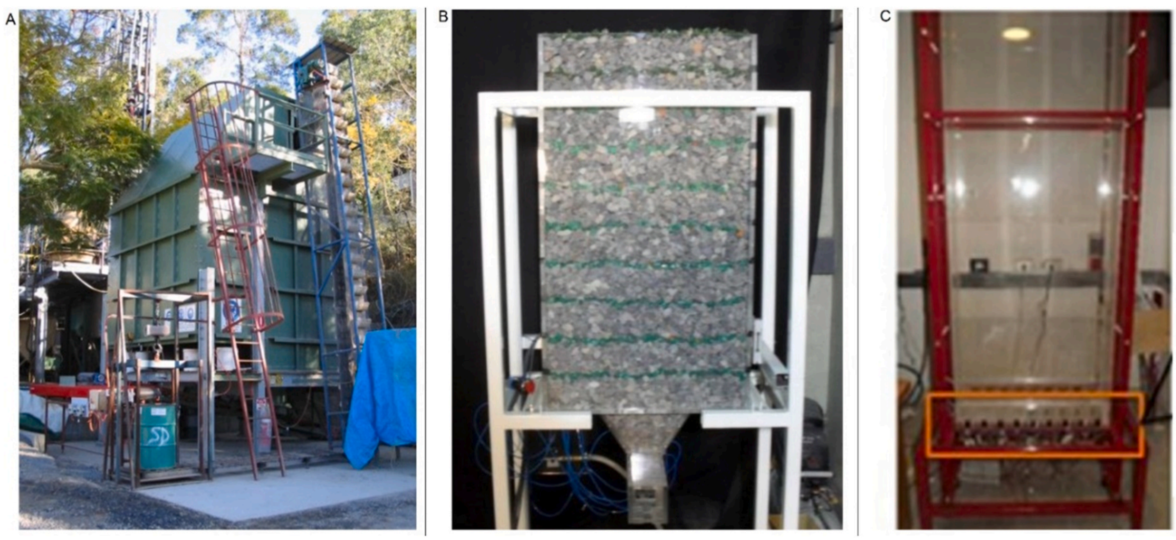

Fig. 6. Physical models used in this study. A: Castro.[4] B: Orellana.[74] C: Castro et al.[7]

Table 1
Model dimensions.

Dimension	Castro[4]	Orellana[74]	Castro et al.[7]
Height [m]	2.4	1	2.5
Width [m]	3.4	0.54	0.7
Length [m]	3.3	0.35	0.23
Granular material	Gravel	Gravel	Sulphide ore

Table 2
Summary of granular material properties.

Parameter	Castro[4]	Orellana[74]	Castro et al.[7]	Glass sphere	Gravel
Real density, kg/m^3	2700	2690	2600	2500	2670
Bulk density, kg/m^3	1900	1610	1420	1150	970
Particle size, mm	[4–14]	[7–35]	[0.8–11]	0.6	[2.36–4.7]
Internal friction angle, °	39	ND	39	27.2	37.9
Angle of repose, °	ND	28.9	29	21.1	40.1

ND: No data.

Table 3
Friction wall angles (°) in the Seditest model.

Materials	Paperboard	Fine sandpaper	Coarse sandpaper
Glass spheres	19.0 ± 0	24.0 ± 0.2	31.5 ± 0.7
Gravel	32.3 ± 0.6	41.3 ± 2.3	42.7 ± 1.5

Table 4
Vertical stress reported in physical models.

Test	Model	Mean vertical stress [kPa]	Standard deviation [kPa]
1	Castro[4]	32.49	15.57
2	Orellana[74]	8.4	6.98
3	Castro et al.[7]	19.65	5.58
4	Seditest gravel (φ_w = 32.3°)	0.48	0.07
5	Seditest gravel (φ_w = 41.3°)	0.38	0.05
6	Seditest gravel (φ_w = 42.7°)	0.36	0.08
7	Seditest glass (φ_w = 19.0°)	0.68	0.01
8	Seditest glass (φ_w = 24.0°)	0.62	0.03
9	Seditest glass (φ_w = 31.5°)	0.54	0.01

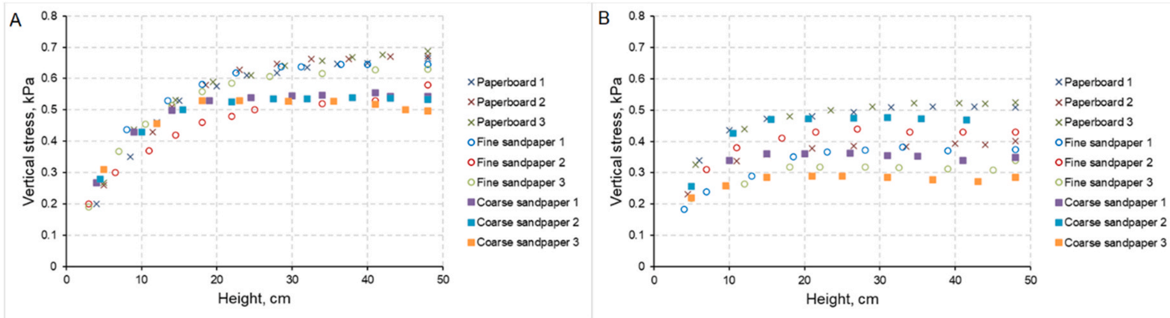

Fig. 7. Vertical stress reported in the Seditest model, 3 replications per test. A: Glass spheres and B: Gravel.

Table 5
Numerical model calibration: static condition.

Parameter	Castro[4]	Orellana[74]	Castro et al.[7]	Seditest Gravel			Seditest Glass Spheres		
				$\varphi_w = 32.3^\circ$	$\varphi_w = 41.3^\circ$	$\varphi_w = 42.7^\circ$	$\varphi_w = 19^\circ$	$\varphi_w = 24^\circ$	$\varphi_w = 31.5^\circ$
Mean vertical stress (experimental)	32.49	8.63	19.65	0.48	0.38	0.36	0.68	0.62	0.54
Mean vertical stress (simulated)	32.44	8.65	19.51	0.48	0.38	0.36	0.68	0.62	0.54
Standard deviation (experimental)	15.57	6.99	5.58	0.07	0.05	0.08	0.01	0.03	0.01
Standard deviation (simulated)	15.62	6.37	5.37	0.08	0.07	0.09	0.05	0.04	0.04
E (%)	99.54	97.21	98.95	54.0	41.8	38.5	71.8	69.1	64.6
s	N[8,7]	N[50,49]	N[4,3]	N[2,0.1]	N[2,0.1]	N[2,0.1]	N[2,0.1]	N[2,0.1]	N[2,0.1]

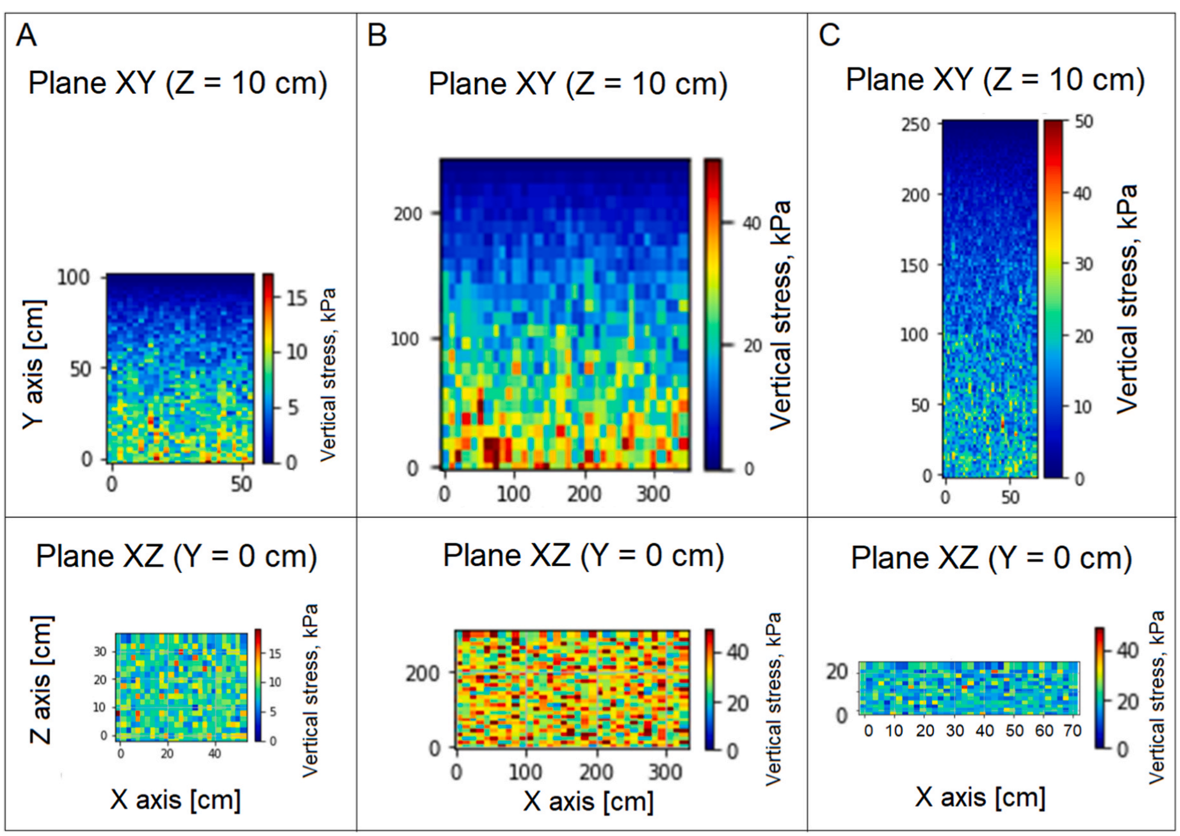

Fig. 8. Simulated vertical stress (color legend in kPa) for tests 1, 2 and 3. A: Test 1. B: Test 2. C: Test 3. (For interpretation of the references to color in this figure legend, the reader is referred to the Web version of this article.)

3.1. Physical models

The data obtained from the physical models were used in this study to calibrate the stress model. Three of the physical models were selected because stress for block caving applications had previously been measured.[4,7,74] Additionally, a fourth physical model (Seditest) was used in this work to vary the effect of the wall friction and material properties.

The setup of the Seditest model consists of an acrylic column shown in Fig. 5, with a height of 50 cm and 10×8 cm^2 square-cross section. At

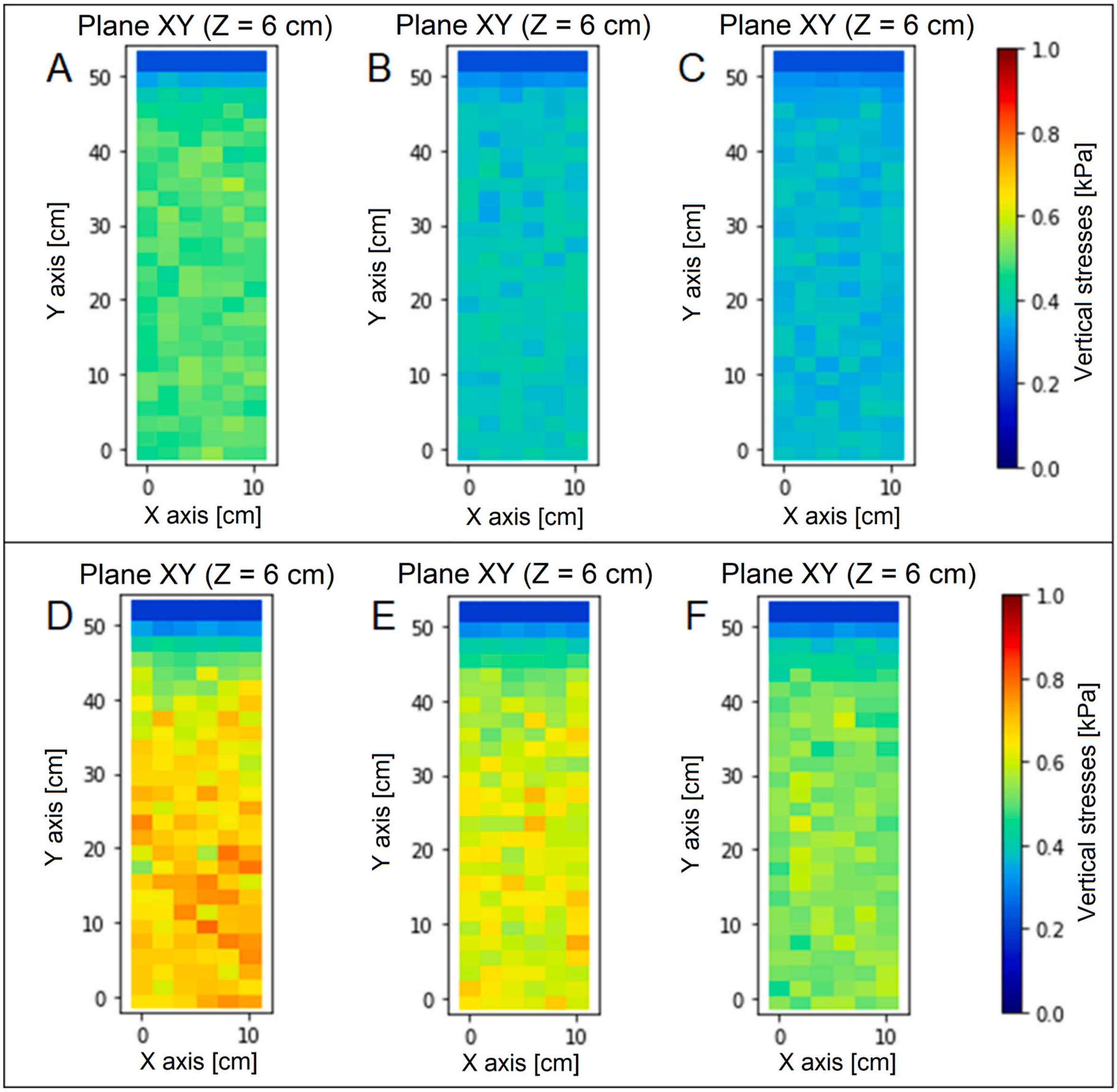

Fig. 9. Simulated vertical stress for the Seditest with gravel in A: Test 4. B: Test 5 and C: Test 6, and glass spheres in D: Test 7. E: Test 8 and F: Test 9.

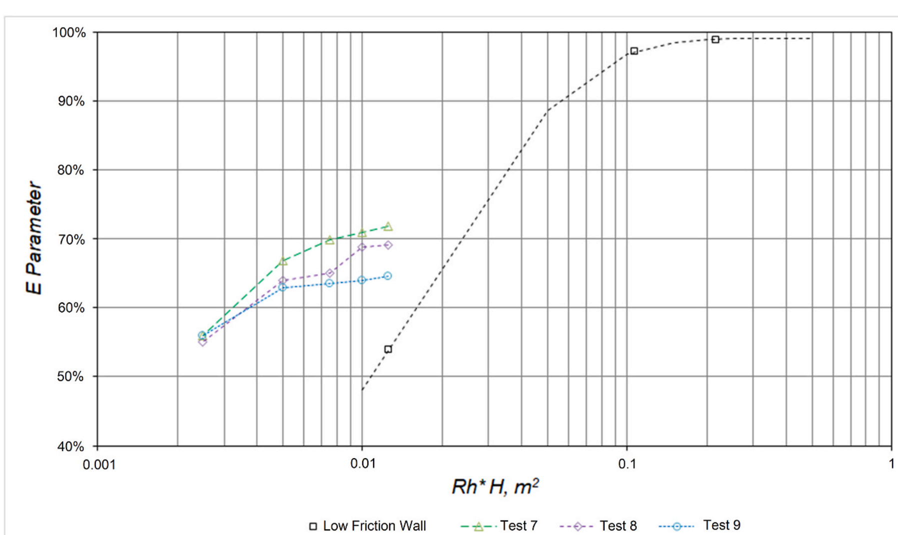

Fig. 10. Model geometry and wall-friction effect on *E*. The low friction wall markers correspond to the physical model of Fig. 6.

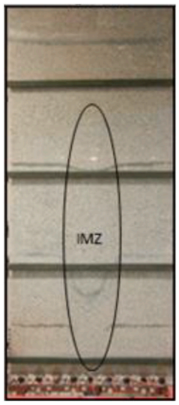

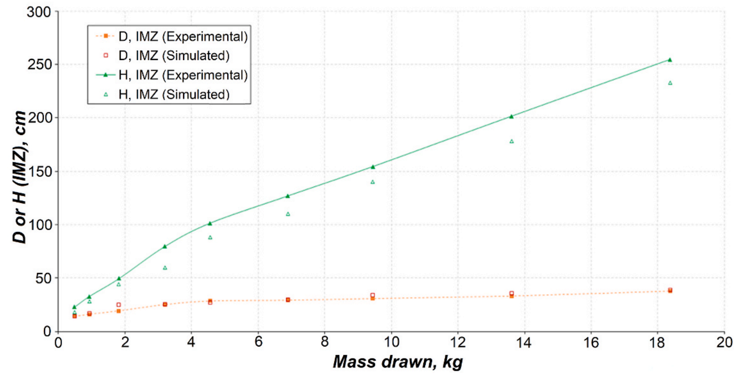

Fig. 11. Isolated extraction used to calibrate numerical parameters during flow.[7]

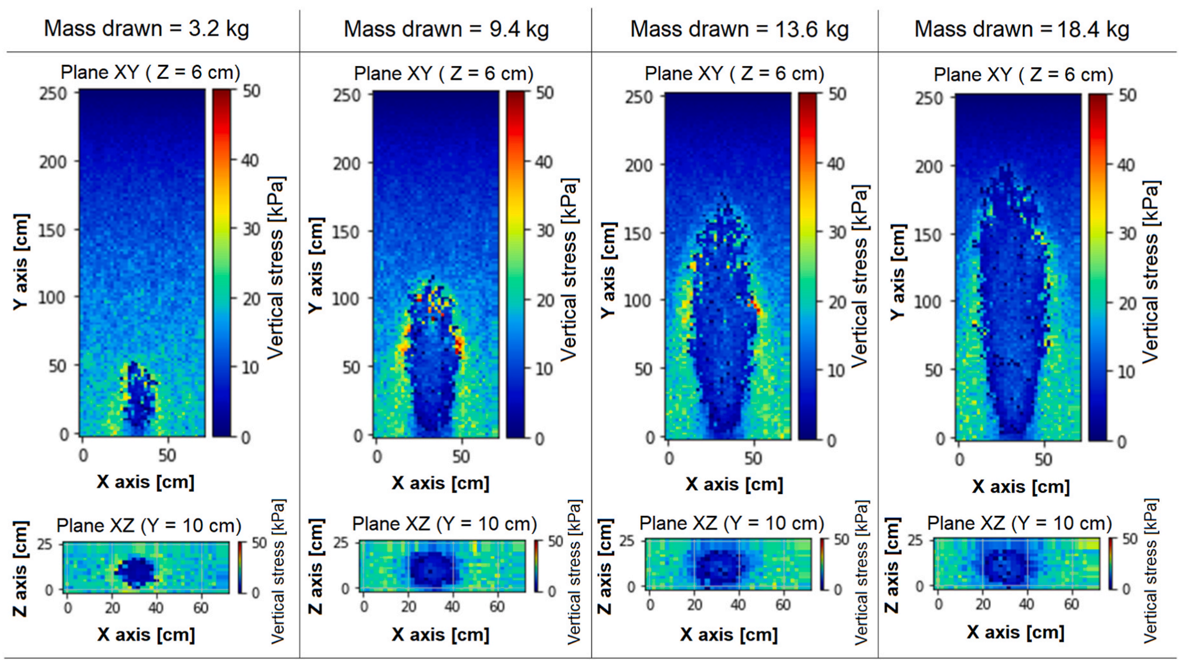

Fig. 12. CA simulation of vertical stresses during isolate draw.

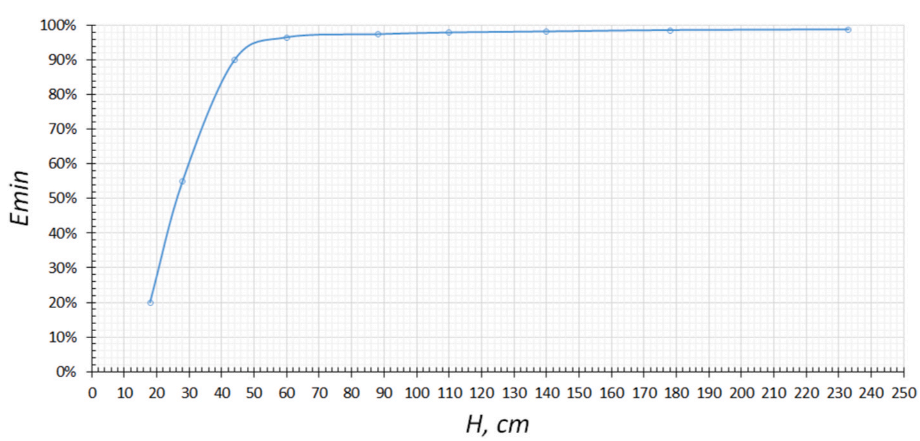

Fig. 13. E_{min} based on IMZ height obtained from isolated experiment by.[7]

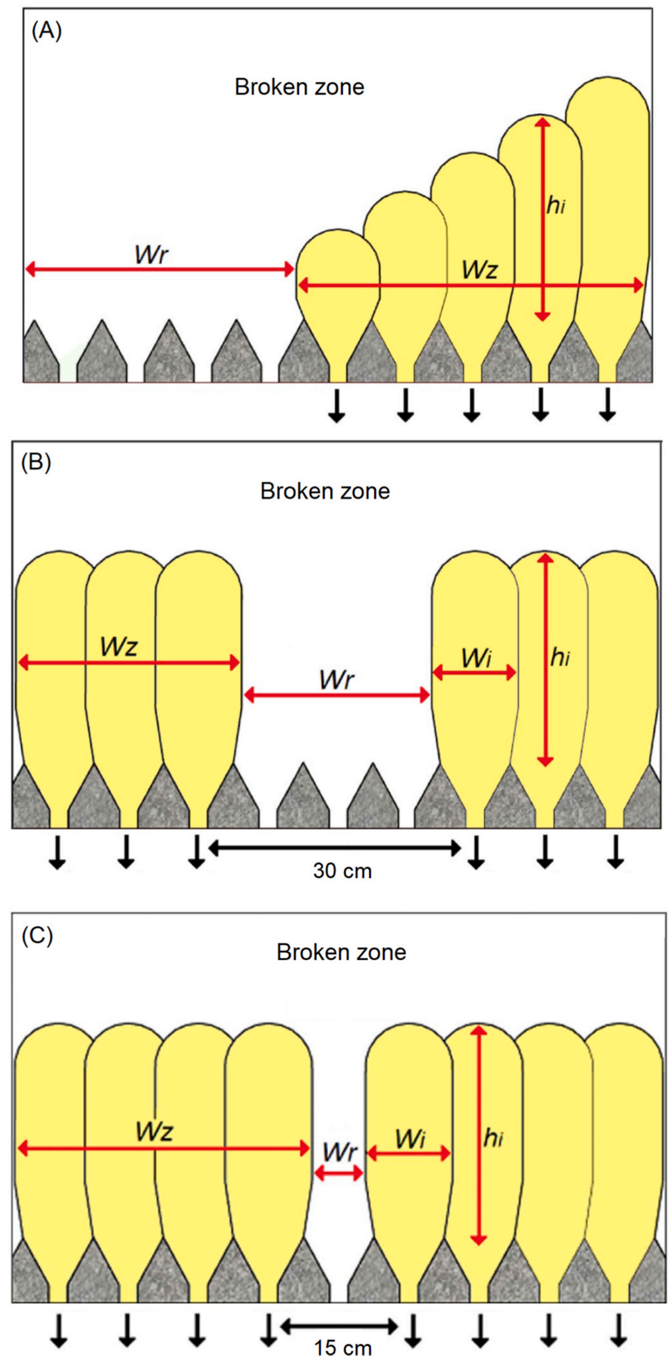

Fig. 14. Experimental setup of different draw strategies (modified from [7]). A. Planel caving strategy. B: Block caving with 30 cm of pillar. C: Block caving with 15 cm of pillar.

the bottom of the column a load sensor (Danfoss MBS 4510-060G2418) is located. A feeder is used to fill the column with the granular material (Fig. 5-B). Glass spheres and gravel were used as granular material. Additionally, three materials were used in the model walls to modify the wall roughness: paperboard, a fine sandpaper, and a coarse sandpaper.

The other three physical models used to calibrate the stress model are presented in Fig. 6. In these models, the vertical stress was measured in the base around drawpoints or over drawbells. All experiments demonstrated high variability of stress measurements. Table 1 indicates the physical model dimensions and granular media used.

Table 2 indicates the material characteristics used in the models of Fig. 6 and the Seditest. In the Seditest, two granular materials were used: glass spheres and gravel. The gravel was previously fragmented and sieved. The real density and bulk density of the material were measured.[75] A simple shear test using a shear box (10×10 cm^2) was used to measure the undrained shear properties.[76]

The friction between the granular materials and the wall materials, φ_w, was measured using the tilting methodology proposed by Nedderman.[77] It is assumed that this value is the static friction wall angle parameter for the maximum angle before sliding. Table 3 shows the friction wall angle obtained for the material used in the Seditest model. The friction wall angles increase as wall roughness increases for all granular materials tested as was expected. The friction wall angles were also reported to be 25°[7] and 19.7°[74] respectively. The friction angle between the wall and the material is higher than the internal friction angle of the glass spheres when coarse sandpaper is used and is also higher for gravel when fine and coarse sandpapers are used.

In the Seditest model, the filling time per test was 2 min. After filling the column, the vertical stress was measured for 10 min, during which no changes of vertical stress measurement were observed. A total of 6 combinations of wall and granular materials were used, each combination was repeated 3 times for a total of 18 tests.

3.2. Stress data

The stress data reported in Castro,[4] Orellana,[74] Castro et al.[7] and Seditest are shown in Table 4. Here the mean vertical stress measured in the static condition (i.e. before flow) is presented.

In the Seditest model, the vertical stress was also measured during filling at different heights. A Janssen effect was observed in all tests. Fig. 7 shows the results of the glass spheres and gravel for all wall materials. The vertical stress measured on glass spheres increased during filling. The effect of the wall roughness is observed between the paperboard and coarse sandpaper material wall. The results of the fine sandpaper showed a high variability; however, the mean stress values fall between the other wall materials. The gravel showed lower vertical stress than glass spheres. The gravel and glass spheres have a similar bulk density (970 and 1150 kg/m^3, respectively), but the glass spheres have lower friction wall angles, which could explain why glass spheres demonstrate higher vertical stress.

3.3. Stress model calibration

The physical models presented in section 3.1 were simulated numerically to calibrate the stress model. The parameter E (Eq. (2)) was calibrated through the mean vertical stress reported whereas the parameter s (Eq. (4)) was calibrated through the standard deviation of the vertical stress reported. The mean square error was minimized to calibrate both parameters (E and s) between the vertical stress from experiments and numerical simulations, using Eq. (6).[78]

$$min \sum_{j=1}^{m} \left(\sigma_{v,exp} - \sigma_{v,sim}\right)^2 \tag{6}$$

Here, $\sigma_{v,exp}$ is the experimental mean vertical stress, and $\sigma_{v,sim}$ is the simulated mean vertical stress in the CA model. Ten simulations were run per test as shown in Table 4. The cell size used is 2x2x2 cm^3 in all tests except in test 1,[4] in which the cell size used was $10\text{x}10 \times 10$ cm^3. The simulation time for the static condition is less than 1 min and approximately 5 min for the draw condition (varying depending on the draw scenario).

First the block model for each test is created which includes the model size and the cell properties (such as cell ID, cell state, cell density, d_{50}). Then, the stresses are calculated in the static condition using the cell densities and equations (1)–(4), in which the equations' parameters are calibrated with experimental data. In the flow condition, gravity flow is simulated first, and then the stresses are calculated as mentioned above.

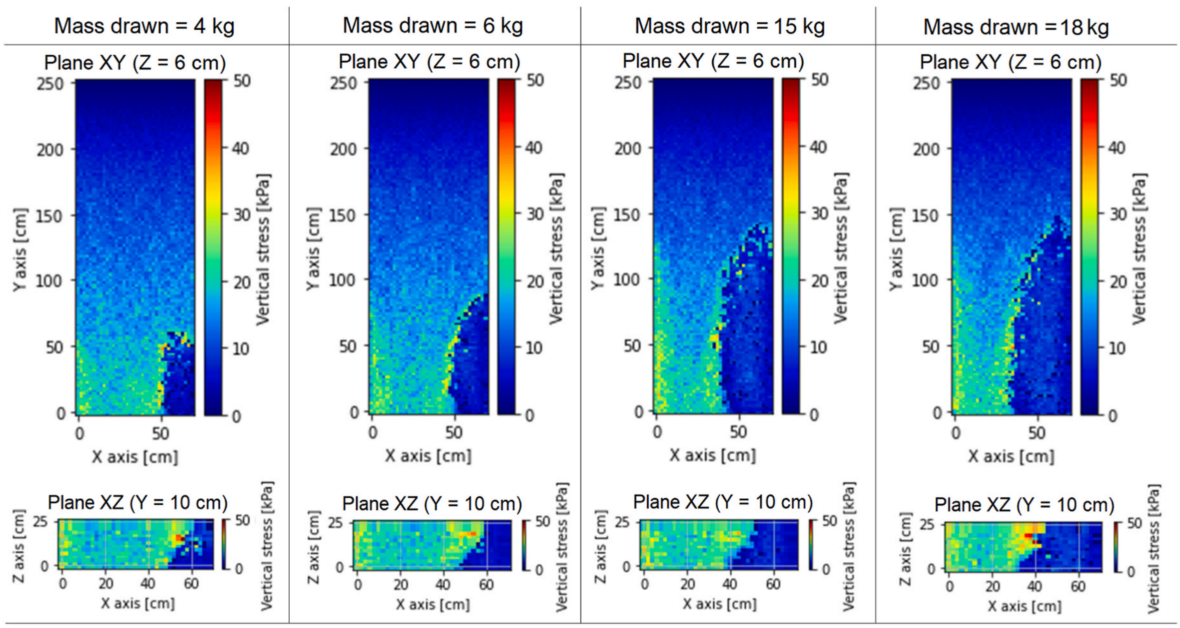

Fig. 15. Vertical stress simulation for panel caving draw strategy.

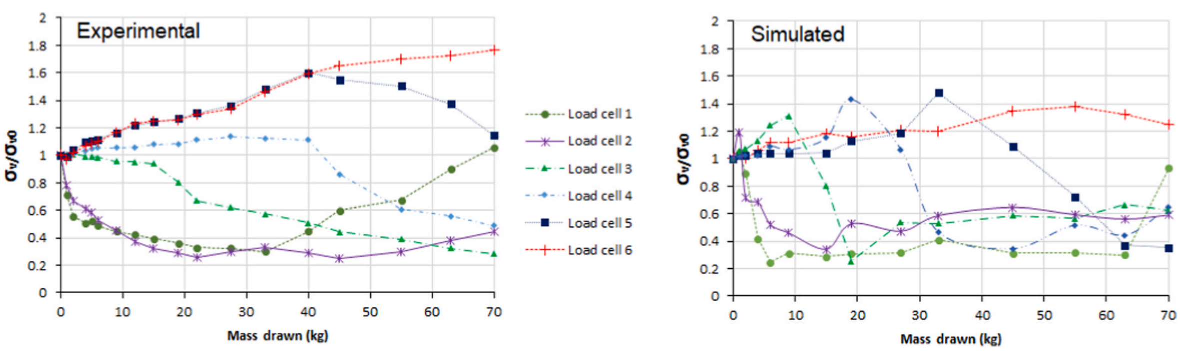

Fig. 16. Experimental and numerical simulation of Panel Caving draw scenario.

4. Results

4.1. Before flow: static calibration

Table 5 shows the experimental and simulated results, as well as the calibrated parameters E and s. Here, the parameter s was modeled using a normal distribution function (Eq. (7);[79]) to obtain the experimental variability of vertical stress. The parameter E increased with the height of the model (H), decreasing its effect as indicated in section 2.1.

$$p(x) = \frac{1}{\sigma\sqrt{2\pi}} exp\left(-\frac{1}{2}\left(\frac{x-\mu}{\sigma}\right)^2\right) \quad \forall x \in \mathbb{R} \tag{7}$$

In this Eq. (7), μ is the mean and σ is the deviation, commonly denoted by $N(\mu, \sigma)$.

Fig. 8 shows the results of the three models (Test 1, 2 and 3) with the calibrated parameters in static condition. The simulated vertical stress increased with depth (Y axis) under a stochastic behavior between cells. In the plan views of Fig. 8 (Plane XY), high vertical stress variability is observed as was expected from experimental results.

Fig. 9 shows the numerical calibration of the Seditest. The E parameter also depends on wall friction at least for a small hydraulic radius. This effect can be observed in Fig. 10, where E is related to geometrical parameters (Rh and H) for gravel and ore materials, which have similar friction angles (37.9° - 39°).

The parameter E increases asymptotically to 100% when Rh and H increased in the geometries modeled. In Fig. 10, the wall friction influenced E (Test 7, 8 and 9), decreasing E when the wall friction increased. The different Rh*H of the Seditest were obtained based on different granular material heights during filling.

4.2. During flow: isolated movement zone calibration

In this section, the parameters E_{min} and R are calibrated as described in Section 2.2. These parameters are calibrated based on Test 1 reported in Castro et al.,[7] where isolated extraction was simulated. The calibrated parameters are determined minimizing the error between simulated and experimental vertical stresses (Eq. (6)), using the parameter $E = 98.95\%$ previously determined. Fig. 11 shows the physical experiment used, and the calibration of the flow zone geometry (diameter and height) simulated in the gravity flow simulator.

The calibrated model of vertical stresses is presented in Fig. 12. Here the growing of the isolated extraction zone (IMZ) can be observed due to ore extraction from the base of the model. The vertical stress decreased in the movement zone (blue ellipse). On the other hand, vertical stress concentrations are observed in the boundary of the IMZ implying more weight transmission to stagnant zones.

This calibration allows the evolution of E_{min} to be determined as function of the height of MZ (Fig. 13) of this setup. The calibrated parameter R is 0.29. Then, it is possible to evaluate the stress logic under different draw conditions using this experimental setup. In Castro et al.[7]

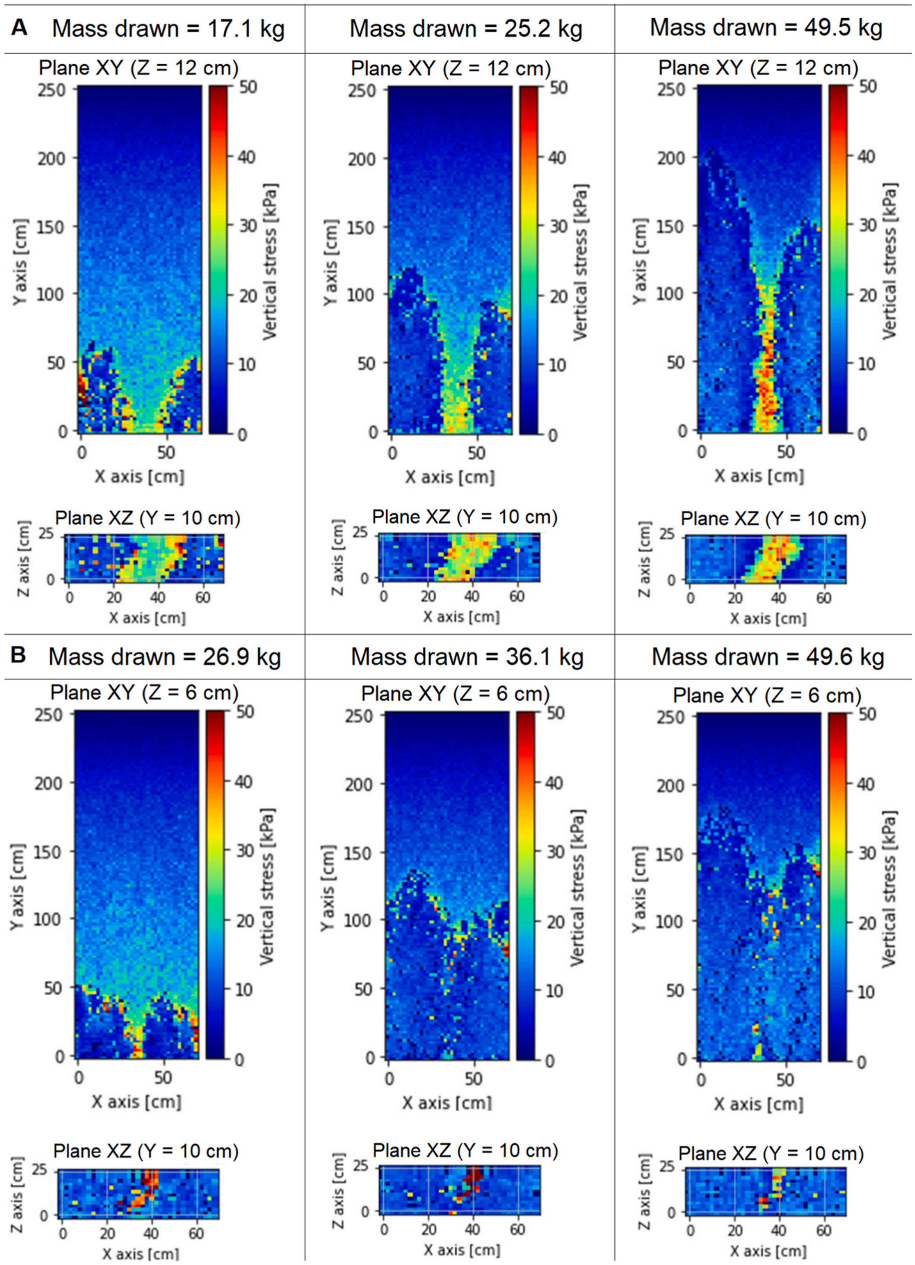

Fig. 17. Vertical stress simulation of Block Caving draw strategy. A: 30 cm of spacing and B: 15 cm of spacing.

different flow scenarios were reported that can be simulated with the calibrated model, $E = 98.95\%$, $R = 0.29$ and E_{min} based on Fig. 13.

5. Experimental validation

Three flow setups were simulated numerically using the stress model, applying the parameters (E, s, E_{min} and R) calibrated in Section 4. These flow experiments included a Panel Caving draw, a Block Caving draw with non-flow zone of 30 cm (spacing between drawpoints), and a Block Caving draw with a non-flow zone of 15 cm, reported in Ref. 7. In the Panel Caving draw, the granular material was extracted continuously from different drawpoints (Fig. 14A). In the Block Caving draw with a non-flow zone (stagnant pillar) of 30 cm, the material was drawn from side drawpoints while the central drawpoints were not extracted (Fig. 14B). In the Block Caving draw with a non-flow zone (stagnant pillar) of 15 cm, the material was also drawn from side drawpoints with a smaller non-flow zone (Fig. 14C).

In Fig. 14, the movement zones generated are indicated in yellow. These zones grow continuously due to ore extraction. The width of the movement zone is denoted by W_Z. *Wi* is the width of the IMZ, *Hi* the height of the IMZ, and *Wr* is the stagnant pillar width. In these experiments, the vertical stresses were measured over the drawbells.

The simulated result of the Panel Caving scenario is presented in Fig. 15. Lower vertical stress is observed (blue color) in the cells located at the top of the model and in the movement zone, while higher stress concentration can be observed in the stagnant zone.

The mean vertical stress is compared between experimental and numerical simulations to analyze the stress model. The mean vertical stress in the numerical model was determined based on five replications per test. The vertical stress in the physical experiments was measured using load cells. The same location of the load cell was used to measure the vertical stress in the numerical model. Fig. 16 shows the experimental and numerical results through the ratio between the vertical stress of each cell at this moment of mass draw (σ_v) and the initial

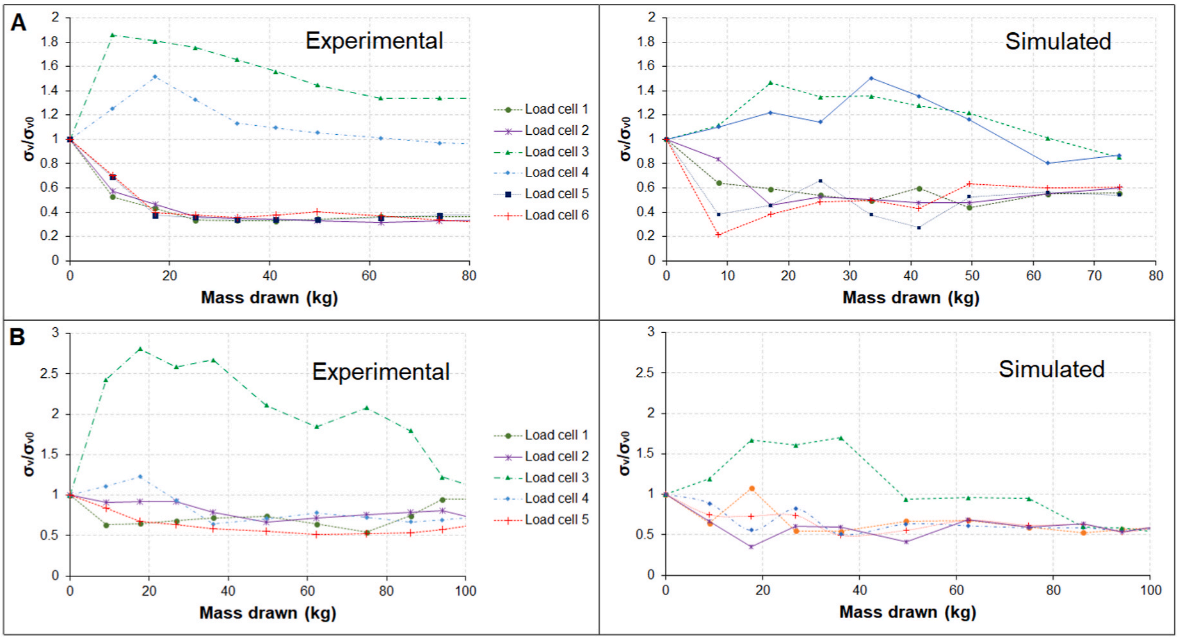

Fig. 18. Experimental and numerical simulation of Block Caving draw scenarios. A: 30 cm of spacing and B: 15 cm of spacing.

vertical stress (σ_{v0}), for six load cells in the Panel Caving scenario. Here, the stress in the movement zone quickly decreased due to draw (load cells 1 and 2) in both the experimental and simulated models. Similarly, the vertical stress is decreased within the movement zone, and this is reflected when the movement zone reaches load cells 3, 4, and 5. On the other hand, the vertical stress is increased in the stagnant zone, until that zone is transformed into a movement zone. This last behavior has also been reported in DEM simulations.[19],[20]

Fig. 17 shows the vertical stress simulated in Block Caving scenarios with a stagnant pillar in the center. The vertical stresses in the movement zones (both sides) decreased during draw, similar to with the Panel Caving draw. On the other hand, in the stagnant zone, the vertical stress increased due to the weight transferred from the movement zones (by parameter R). This weight was transferred to the stagnant zone and continued to the bottom of the model. There are higher stress concentrations in a smaller area when a non-flow zone of 15 cm is utilized (Fig. 17B; Plane XZ: mass draw 26.9 and 36.1 kg). Then, the vertical stress in this zone decreased because the cells are reached by the movement zone (Fig. 17; mass draw 49.6 kg).

Fig. 18 shows the experimental and numerical results using the ratio between the vertical stress at the moment of draw and the initial vertical stress of the Block Caving scenarios. Here, six load cells were used in the experiment with a stagnant pillar of 30 cm, while five load cells were used in the experiment with 15 cm. In the Block Caving scenario with 30 cm of non-flow zone (Fig. 18A), there are two load cells located in the stagnant zone: load cells 3 and 4. These load cells showed higher vertical stress at draw in comparison to their initial vertical stress in both the numerical and experimental models. Likewise, in the Block Caving scenario with 15 cm of non-flow zone (Fig. 18B) — with only one load cell located in the stagnant zone: load cell 3 — this load cell had higher vertical stress at draw compared with its initial vertical stress in the experiment and also in the numerical model. The simulated vertical stress in the stagnant zones of both scenarios were of a smaller magnitude than what was experimentally measured. On the other hand, the vertical stress of the movement zones of the experiments and simulations is similar, decreasing due to draw.

The mean errors between the experimental and simulated vertical stress are 1.53 kPa, 2.16 kPa and 5.18 kPa, respectively. These errors are assumed to be acceptable by the authors because of the natural stress variability in granular media and the experimental variability (5.58 kPa). The Block Caving draw scenario with a non-flow zone of 15 cm showed the highest error mainly due to the differences in load cell 3. In that scenario, load cell 3 did not simulate high vertical stress probably because the experiment used to calibrate the parameter R did not demonstrate stress concentration in the stagnant zone. However, the stress model can replicate vertical stress concentrations in the stagnant zones and — with even more accuracy — stress relaxation in the movement zones.

6. Conclusions

In this work, a stress model is presented to simulate vertical stress in granular materials using a CA. The CA used allows gravity flow to be simulated quickly and precisely in large scale models as required by cave mining. Then, the stress in static and dynamic flow conditions can be simulated at large scale when modeled though a gravity flow simulator based on CA. The proposed stress model was calibrated with different experiments at laboratory scale in which a high level of accuracy was observed for different material media and model geometries in static conditions. The parameter E is constant for the same type of material, problem geometry and mesh selected (cell sizes). However, this parameter increased when the height of the model is increased as in cave mining during caving propagation. The stress model also simulated flow conditions through the parameters R and E_{min}. These parameters were calibrated and compared under different flow scenarios, showing good results based on the expected variability of the experimental setup used. Then, our vertical stress model with the flow simulator based on CA has the potential to be applied at block caving scale once the model parameters are defined.

Declaration of competing interest

The authors declare the following financial interests/personal relationships which may be considered as potential competing interests:

Raul Castro reports financial support was provided by Comisión Nacional de Investigación Científica y Tecnológica. Rene Gomez reports financial support was provided by Comisión Nacional de Investigación Científica y Tecnológica.

Acknowledgments

This work was funded by the CONICYT PFCHA/DOCTORADO BECAS CHILE/2018–21180046 and by the Vicerrectoría de Investigación y Desarrollo of the Universidad de Concepción VRID NO2200.095.090-INI. This paper/work was partially funded by the CONICYT/PIA Project AFB180004. Authors thank Diane Greenstein for her support in editing.

References

1 Killion ME. Design pressures in circular bins. *J Struct Eng*. 1985;111(8):1760–1774.
2 Mahmoodi F. *Compression Mechanics of Powders and Granular Materials Probed by Force Distributions and a Micromechanically Based Compaction Equation*. PhD Thesis. Uppsala: Universitatis Upsaliensis; 2012.
3 Bock S, Prusek S. Numerical study of pressure on dams in a backfilled mining shaft based on PFC3D code. *Comput Geotech*. 2015;66:230–244.
4 Castro RL. *Study of the Mechanisms of Gravity Flow for Block Caving*. PhD Thesis. Brisbane: University of Queenslad; 2007.
5 Pierce ME. *A Model for Gravity Flow of Fragmented Rock in Block Caving Mines*. PhD Thesis. Brisbane: University of Queensland; 2009.
6 Pierce ME. Forecasting vulnerability of deep extraction level excavations to draw-induced cave loads. *J Rock Mech Geotech Eng*. 2019;11(3):527–534.
7 Castro R, Gómez R, Pierce M, Canales J. Experimental quantification of vertical stresses during gravity flow in block caving. *Int J Rock Mech Min Sci*. 2020;127:104237.
8 Janssen HA. Experiments regarding grain stress in soils. *Zeitschrift Des Vereines Deutscher Ingeniure*. 1985;39(35):1045–1049. Translated from German by W. Hustrulid and N. Krauland in Proceedings of the Massmin 2004, Santiago. p. 293-1049.
9 Cundall P, Strack O. A discrete numerical model for granular assemblies. *Geotechnique*. 1979;29:47–65.
10 Landry JW, Grest GS, Silbert LE, Plimpton SJ. Confined granular packings: structure, stress, and forces. *Phys Rev*. 2003;67(4), 041303.
11 Zhou YC, Xu BH, Zou RP, Yu AB, Zulli P. Stress distribution in a sandpile formed on a deflected base. *Adv Powder Technol*. 2003;14(4):401–410.
12 Landry JW, Grest GS, Plimpton SJ. Discrete element simulations of stress distributions in silos: crossover from two to three dimensions. *Powder Technol*. 2004;139(3):233–239.
13 Kobyłka R, Molenda M. DEM modelling of silo load asymmetry due to eccentric filling and discharge. *Powder Technol*. 2013;233:65–71.
14 Matchett AJ, Langston PA, McGlinchey D. A model for stresses in a circular silo with an off-centre circular core, using the concept of a principal stress cap: solution for a completely filled silo and comparison with Janssen and DEM data. *Chem Eng Res Des*. 2015;93:330–348.
15 Wang P, Zhu L, Zhu X. Flow pattern and normal pressure distribution in flat bottom silo discharged using wall outlet. *Powder Technol*. 2016;295:104–114.
16 Zhao H, An X, Wu Y, Qian Q. DEM modeling on stress profile and behavior in granular matter. *Powder Technol*. 2018;323:149–154.
17 Kobyłka R, Molenda M, Horabik J. Loads on grain silo insert discs, cones, and cylinders: experiment and DEM analysis. *Powder Technol*. 2019;343:521–532.
18 Hadjigeorgiou J, Lessard JF. Numerical investigations of ore pass hang-up phenomena. *Int J Rock Mech Min Sci*. 2007;44(6):820–834.
19 Hancock W. *Gravity Flow of Rock in Caving Mines: Numerical Modelling of Isolated, Interactive and Non-ideal Draw*. PhD Thesis. Brisbane: University of Queensland; 2013.
20 Pierce ME, Cundall PA, Van Hout GJ, Lorig L. PFC3D modeling of caved rock under draw. In: *Numerical Modeling in Micromechanics via Particle Methods*. 2017:211–217.
21 Cid P. *Gravity Flow Simulation in a Drawbell Using Discrete Element Method. Bachelor Degree*. Concepción: Universidad de Concepción; 2019 (in spanish).
22 Guest AR, van Hout GJ, von Johannides A, Scheepers LF. An application of linear programming for block cave draw control. In: *Massmin 2000 Proceeding*. 29 October – 2 November 2000:461–468. Brisbane.
23 Sharrock G, Beck D, Booth G, Sandy M. Simulating gravity flow in sub-level caving with cellular automata. In: *Massmin 2004 Proceeding*. 22-25 August 2004:189–194. Santiago.
24 Castro RL, Whiten WJ. *A New Cellular Automaton to Model Gravity Flow in Block Caving Based on Physical Modelling Observations*. 2007:233–241.
25 Rojas E, Molina R, Bonani A, Constanzo H. The pre-undercut caving method at the El Teniente mine, codelco Chile. In: *Massmin 2000 Proceeding*. 29 October – 2 November 2000:261–266. Brisbane.
26 Karzulovic A. *Conceptual Field Stress Model in El Teniente Mine*. 2006 (In Spanish, internal report).
27 Xia ZY, Tan ZY, Zhang L. Instability mechanism of extraction structure in whole life cycle in block caving mine. *Geofluids*. 2021.
28 Hooker VE, Bickel DL. *Overcoring Equipment and Techniques: Used in Rock Stress Determination*. vol. 8618. US Bureau of Mines; 1974.
29 Brady BHG, Brown ET. Premining state of stress analysis. In: *Rock Mechanics for Underground Mining*. 2004:142–164.
30 Martin CD, Kaiser PK, McCreath DR. Hoek-Brown parameters for predicting the depth of brittle failure around tunnels. *Can Geotech J*. 1999;36(1):136–151.
31 Gonzales R, Munoz R, Vallejos J, Delonca A. Characterisation and monitoring of the stress state of production pillars at El Teniente Mine. In: *Seventh International Conference & Exhibition on Mass Mining, Massmin 2016*. 9-11 may 2016:197–201. Sydney.
32 Febrian I, Yudanto W, Rubio E. Application of convergence monitoring to manage induced stress by mining activities at PT Freeport Indonesia deep ore zone mine. In: *Massmin 2004 Proceeding*. 2004:269–272. Santiago; 22-25 August 2004.
33 Xia ZY, Tan ZY. Study on instability mechanism of extraction structure under undercut space based on thin plate theory in block caving method. *Shock Vib*. 2021.
34 Sahupala H, Brannon C, Annavarapu S, Osborne K. Recovery of extraction pillars in the deep ore zone (DOZ) block cave, PT freeport Indonesia. In: *Massmin 2008, 5th International Conference & Exhibition on Mass Mining. Lulea*. 9-11 June 2008:191–192.
35 Orellana M, Cifuentes C, Díaz J. Caving experiences in Esmeralda sector, El Teniente mine. In: *Caving 2014, 3rd Symposium on Block and Sublevel Caving*. 5-6 June 2014:78–90. Santiago.
36 Litwiniszyn J. Stochastic methods in mechanics of granular bodies. In: *Stochastic Methods in Mechanics of Granular Bodies*. Vienna: Springer; 1974:5–9.
37 Osinov VA. A model of a discrete stochastic medium for the problems of loose material flow. *Continuum Mech Therm*. 1994;6(1):51–60.
38 Mullins WW. Stochastic theory of particle flow under gravity. *J Appl Phys*. 1972;43(2):665–678.
39 Caram HS, Hong DC. Diffusing void model for granular flow. *Mod Phys Lett B*. 1992;6(13):761–771.
40 Chen G. Stochastic modeling of rock fragment flow under gravity. *Int J Rock Mech Min Sci*. 1997;34(2):323–331.
41 Kamrin K, Bazant MZ. Stochastic flow rule for granular materials. *Phys Rev*. 2007;75(4), 041301.
42 Liu CH, Nagel SR, Sche, et altten TA. Force fluctuations in bead packs. Science. 1995; 269(5223):513-515.
43 Coppersmith SN, Liu CH, Majumdar S, Narayan O, Witten TA. Model for force fluctuations in bead packs. *Phys Rev*. 1996;53(5):4673.
44 Hemmingsson J, Herrmann HJ, Roux S. Vectorial cellular automaton for the stress in granular media. *J Phys*. 1997;7(2):291–292.
45 Jolley D. Computer simulation of movement of ore and waste in an underground mining pillar. *Can Min Metall Bull*. 1968;61(675):854.
46 Calderon C, Alfaro M, Saavedra J. Computational model for simulation and visualization of gravitational flow. In: *Massmin 2004 Proceeding*. August 2004:185–188. Santiago; 22-25.
47 Castro RL, Gonzalez F, Arancibia E. Development of a gravity flow numerical model for the evaluation of drawpoint spacing for block/panel caving. *J S Afr Inst Min Metall*. 2009;109(7):393–400.
48 Gibson WH. Stochastic models for gravity flow: numerical considerations. In: *Caving 2014, 3rd Symposium on Block and Sublevel Caving*. 5-6 June 2014:337–347. Santiago.
49 Hebert Y, Sharrock G. Three-dimensional simulation of cave initiation, propagation and surface subsidence using a coupled finite difference-cellular automata solution. In: *Caving 2018, Proceeding of the Fourth International Symposium on Block and Sublevel Caving. Adelaine*. 2018:151–166, 30 August – 1 September 2018.
50 Kothari UC, Sinaga FM, Tshisens JN. Understanding surface subsidence from a block cave by comparing InSar data with 3D numerical modelling. *Massmin 2020, Eight International Conference & Exhibition on Mass Mining*. 9-11 December 2020:318–326. Santiago.
51 Webster S, Samosir E, Wyllie A. Learning from mining cave extension at Northparkes Mines and new technology to improve the value of future cave designs. *Massmin 2020, Eight International Conference & Exhibition on Mass Mining*. 9-11 December 2020:92–102. Santiago.
52 Castro R, Gómez R, Arancibia L. Fine material migration through cellular automata. *Granul Matter*. 2022;24(1):1–11.
53 Laubscher DH. Draw control. In: *Cave Mining Handbook*. 2000:111–115.
54 Power G. Full scale SLC draw trials at ridgeway gold mine. In: *Massmin 2004 Proceeding*. 22-25 August 2004:225–230. Santiago.
55 Garcés D. *Gravity Flow Study of Broken Material through Intelligent Markers. Bachelor Degree*. Santiago: Universidad de Chile; 2015 (in Spanish).
56 Dunstan G. The thruth is stranger than fiction – the story of ridgeway gold mine. In: *Seventh International Conference & Exhibition on mass mining, Massmin 2016*. 9-11 may 2016:19–30. Sydney.
57 Power GR, Campbell AD. Modelling of real-time marker data to improve operational recovery in sublevel caving mines. In: *Seventh International Conference & Exhibition on Mass Mining, Massmin 2016*. 9-11 may 2016:105–110. Sydney.
58 Brunton I, Leet JL, Thornhill T. Fragmentation prediction and assessment at the ridgeway deeps and cadia east cave operation. In: *Seventh International Conference & Exhibition on mass mining, Massmin 2016*. 9-11 may 2016:151–160. Sydney.
59 Hocking R, Fargher M, Chester C. Marker design and calibration for Carrapateena sub level and block cave with a focus on fines migration and far field Flow. In: *Massmin 2020, Eight International Conference & Exhibition on Mass Mining*. 9-11 December 2020:489–504. Santiago.
60 Hollins B, Tucker J. Draw point analysis using a marker trial at the perseverance nickel mine, leinster, western Australia. In: *Massmin 2004 proceeding*. 22-25 August 2004:498–502. Santiago.
61 Frisch U, Hasslacher B, Pomeau Y. Lattice-gas automata for the Navier-Stokes equation. *Phys Rev Lett*. 1986;56(14):1505.
62 Psakhie SG, Horie Y, Ostermeye, et alek S. Movable cellular automata method for simulating materials with mesostructure. Theor Appl Fract Mech. 2001; 37(1-3):311-334.
63 Jasti VK, Higgs CF. A fast first order model of a rough annular shear cell using cellular automata. *Granul Matter*. 2010;12(1):97–106.
64 Désérable D, Dupont P, Hellou M, Kamali-Bernard S. Cellular automata in complex matter. *Complex Syst*. 2011;20(1):67.

65 Tejchman J. Simulations of flow pattern with cellular automaton. In: *Confined Granular Flow in Silos*. Heidelberg: Springer; 2013:455–492.
66 Tucker GE, McCoy SW, Hobley DE. A lattice grain model of hillslope evolution. *Earth Surf Dyn*. 2018;6(3):563–582.
67 Feng XT, Pan PZ, Zhou H. Simulation of the rock microfracturing process under uniaxial compression using an elasto-plastic cellular automaton. *Int J Rock Mech Min Sci*. 2006;43(7):1091–1098.
68 Yan F, Pan PZ, Feng XT, Li SJ. The continuous-discontinuous cellular automaton method for elastodynamic crack problems. *Eng Fract Mech*. 2018;204:482–496.
69 Pan PZ, Yan F, Feng XT, Wu Z, Qiu S. Modeling of an excavation-induced rock fracturing process from continuity to discontinuity. *Eng Anal Bound Elem*. 2019;106: 286–299.
70 Zuriguel I, Mullin T, Rotter JM. Effect of particle shape on the stress dip under a sandpile. *Phys Rev Lett*. 2007;98(2), 028001.
71 Esterhuizen GS, Rachmad L, Potapov AV, Nordell LK. Investigation of swell factor in a block cave draw column. In: *Massmin 2004 Proceeding*. August 2004:215–219. Santiago; 22-25.
72 Dorador L, Eberhardt E, Elmo D, Norman B, Aguayo A. Assessment of broken ore density variations in a block cave draw column as a function of fragment size distributions and fines migration. In: *Caving 2014, 3rd Symposium on Block and Sublevel Caving*. 5-6 June 2014:109–117. Santiago.
73 Dorador L, Eberhardt E, Elmo D. Procedure for estimating broken ore density distribution within a draw column during block caving. *Min Technol*. 2021;130(3): 131–145.
74 Orellana LF. *Continuous Mining System Evaluation of Design Variables from Experiments*. Santiago: Master thesis. Universidad de Chile; 2012 (in Spanish).
75 ASTM. *Standard Test Method for Specific Gravity and Absorption of Coarse Aggregate*. 2021.
76 ASTM D 3080-04. *Standard Test Method for Direct Shear Test of Soils under Consolidated Drained Conditions*. vol. 4. Conshohocken, PA: ASTM Int.; 2004:1–7.
77 Nedderman RM. *Statics and Kinematics of Granular Materials*. Cambridge University Press; 2005.
78 Moré JJ, Sorensen DC. Computing a trust region step. *SIAM J Sci Stat Comput*. 1983;3: 553–572.
79 Lapin LL. *Probability and Statistics for Modern. Engineering*. Boston: Thomson information/publishing group; 1990.